Current Research (2018) Newfoundland and Labrador Department of Natural Resources Geological Survey, Report 18-1, pages 15-30

ASSESSING THE APPLICABILITY OF UNMANNED AERIAL VEHICLE (UAV) DATA IN ENVIRONMENTAL MONITORING OF COASTAL ENVIRONMENTS: ST. DAVID'S, NEWFOUNDLAND

M. Irvine, G. Roberts and L. Oldham[1]
Terrain Sciences and Geoscience Data Management Section
[1]Department of Earth Sciences, Memorial University of Newfoundland, St. John's, NL, A1B 3X5

ABSTRACT

Assessment of coastal erosion, terrain stability, and flood-risk mapping require high-resolution datasets over multiple years. Methods have been developed and assessed to: a) capture and process UAV data; b) quantify the overall changes in environment, measured over a fixed period of time; c) identify the processes causing landscape change, and d) delineate hazard-prone areas that could be affected by coastal flooding.

The coastal town of St. David's in western Newfoundland was chosen as a case study. A quadcopter UAV was used to acquire overlapping (80%) air photographs in 2016 and 2017, and photogrammetric processing software was used to create a Digital Surface Model (DSM), an orthophotograph and a 3-D model, having a ground resolution of 1.4 cm. Positional accuracy was 6.07 cm, and was improved by the inclusion of 17 control points, surveyed in the field with a Real Time Kinematics (RTK) system. Comparisons of the DSM to ground-surveyed topographic data allowed for the computation of yearly erosion rates of 52 cm per year (cm/a) along the clifftop. Areas of accelerated elevational gain or loss between 2016 and 2017 were determined and the influential erosional agents were identified as surface water, groundwater and wind. Detailed examination, facilitated by the high resolution of the DSM, enabled the delineation of areas susceptible to flooding by the end of the present century. The results demonstrate the applicability of UAVs for measuring and investigating coastal change, and mapping hazard-prone areas.

INTRODUCTION

There is documented history of landscape hazards in Newfoundland and Labrador (*see* Batterson *et al.*, 2006), including terrain instability, erosion and flooding, particularly along the coast and in river valleys. The authors document over 290 geologically related events in the Province, with 160 deaths, as well as personal injury, infrastructure damage and property loss, attributed to landscape hazards.

Geographic, climatic, and geological characteristics variously influence the risk level of landscape hazards. For instance, the coastline between Daniel's Harbour and Green Point on the Great Northern Peninsula is vulnerable to rapid slope movement, as evident by landslide scars in coastal cliffs formed from thick unconsolidated glacial and post-glacial sediment (M. Batterson, personal communication, 2017; Plate 1). As well as such landslide events, unconsolidated coastlines are being eroded at a continuous rate, which poses a threat to infrastructure including roads, trails, build-

Plate 1. *View of historic (arrows) and recent (2007 and 2013) landslide scars (outlined in red) in Daniel's Harbour. After the 2007 landslide, 23 households, secondary roads and the highway were relocated to more stable terrain.*

ings and cemeteries (Plate 2). Yearly rates of erosion of more than 50 cm per year (cm/a) have been recorded along exposed coastal cliffs, including at Parsons Pond on the Great Northern Peninsula (Irvine, 2015). Flooding of low-lying terrain has resulted in infrastructure damage and property loss, and storms have changed beach topography; Placentia has a history of infrastructure damage from high-water levels in the estuary and the outer beach (Batterson *et al.*, 1995; Plate 3A, B).

Increased encroachment of development into coastal areas, and changing environmental conditions, will increase the exposure to, and risk of, landscape hazards. Parts of the Province are experiencing uplift, and others subsidence, resulting in relative sea-level rise predictions ranging from 80 cm in northern Labrador to 100 cm or more on the Avalon, by 2099 (Batterson and Liverman, 2010). This, in combination with projected climate changes for the Province, such as increases in precipitation intensity and rates (Finnis, 2013) will accelerate erosion rates and the increase the risk of floods.

There is a need for high-resolution and accurate data of the morphology and characteristics of land surfaces, collect-

Plate 2. *A) Erosion of the unconsolidated slope, landward of a new housing development in Conception Bay South on the Avalon Peninsula, resulted in the closure of a walking trail shortly after its construction; B) In the winter of 2017, the peat cliff along Shoal Point, on the Port au Port Peninsula, eroded and a shed fell off the cliff (circled); C) Coastal erosion has threatened a portion of the main road in Grand Beach, Burin Peninsula; D) Erosion of the coastal cliff at Parson's Pond, on the Great Northern Peninsula, is compromising the stability of the gravel parking lot. Large boulders have been placed to discourage access to the cliff edge.*

Plate 3. *A) View of the low-lying community of Placentia, showing the outer beach and estuary areas; B) Outer beach area of Placentia showing the same area of the main beach and boardwalk, before (left) and after (right) a storm surge in 2013 that coincided with a high tide. Note the extensive damage to the boardwalk, and the amount of beach material that was moved.*

ed over multiple years. Interpretation of these data will improve the understanding of 1) how areas are changing, 2) what areas are most vulnerable to landscape hazards, and 3) the implications of changing environmental conditions. The integration of landscape-change information into planning, decision making, and the establishment of policies and regulations, will serve to discourage or modify future development in hazardous environments, and better anticipate the implications of landscape change in existing high-risk areas.

Remote-sensing and ground-based techniques have been applied to collect detailed topographic data. Sallenger *et al.* (2003) used Lidar to map changes in beach topography along the North Carolina coast and Razak *et al.* (2011) examined high-density airborne laser-scanning data to identify and classify landslides in southern France. Comparison of decadal aerial photographs can detect landslides (Italy; Fiorucci *et al.*, 2011) and coastal erosion (Newfoundland; Forbes *et al.*, 1995). Topographic surveying using Real Time Kinematics (RTK) has been used to measure coastal change (*see* Dail *et al.*, 2000; Irvine, 2015; Watton, 2016).

METHODS USED TO COLLECTED TOPOGRAPHIC DATA

Recent advances in Unmanned Aerial Vehicle (UAV) technology, and in data-collection applications and processing, allow for investigation of the use of this technology in surficial mapping, environmental monitoring, and hazard assessment. Advantages of UAV image acquisition and processing include detailed ground resolution (Westoby *et al.*, 2012); the capability to fly on demand (Lucieer *et al.*, 2014); low-flight altitudes (Ajayi *et al.*, 2017); low cost (Westoby *et al.*, 2012; Mancini *et al.*, 2013); ease of use (Harwin and Lucieer, 2012); the capability to access inaccessible areas (Kršák *et al.*, 2016); and the non-destructive collection of data (Pineux *et al.*, 2017). Highly accurate models can be created in software packages using Structure from Motion (SfM), a photogrammetric technique that enables the creation of 3-D imagery from 2-D photographs, using algorithms to detect matching points between images (Westoby *et al.*, 2012).

OBJECTIVES

This study investigates how UAV technology using SfM can capture detailed topographic data, suitable for environmental monitoring and hazard assessments. There are two main objectives:

1) To develop methods to obtain accurate elevation data, and compare multi-date imagery to detect and measure temporal changes in landscape morphology; and
2) To assess the applicability of the methods to:
   - Quantify clifftop erosion and its spatial distribution,
   - Determine morphological changes of cliff faces,
   - Identify processes causing landscape change, and
   - Delineate flood-prone areas.

LOCATION – ST. DAVID'S

To demonstrate and evaluate the UAV methods, an actively eroding, unconsolidated cliff and adjacent low-lying area in St. David's, western Newfoundland were selected (Figure 1). The cliff is composed of interbedded medium to coarse sand and silt, and pockets of gravel containing cobbles and boulders with an overlying organic layer. The beach is narrow (about 15 m), and is composed of poorly sorted rounded boulders, gravel and sand. North of the cliff, at the mouth of the Crabbes River, several sheds and a road have been built on low-lying terrain, and a wharf that provides anchorage for fishing boats. Large boulders have been placed on the beach and at the river mouth, to decrease the impact of flooding and erosion. The cliff is continuously eroding, as observed from fresh gullies, rills, overhangs and colluvium. A road runs parallel to the clifftop within 5 m of the cliff edge, and a historic graveyard having headstones dating back to 1866, is located at the northern end of the cliff.

The site has been surveyed as part of a systematic, long-term coastal monitoring program (Irvine, 2015). In 2013, Real Time Kinematic (RTK) equipment was used to collect accurate (centimetre-scale) location data of the position of the cliff edge, and these data are used in the current clifftop-erosion calculations.

METHODS

UAV Aerial Survey

A quadcopter UAV was flown over the St. David's study area in 2016 and 2017 (Table 1, Plate 4). Traverses were designed using the Maps Made Easy web application, flown on auto-pilot, with an 80% image overlap and a vertically oriented camera; manual mode was used to capture oblique photographs. Photos were acquired during periods of mini-

Table 1. Summary statistics describing the 2016 and 2017 flights

	2016	2017
UAV	DJI Inspire 1	DJI Inspire 2
Camera focal length (mm)	3.61	8.8
Flying altitude (m)	80	62
Number of Markers	4	21
Ground resolution (cm)	2.91	1.4

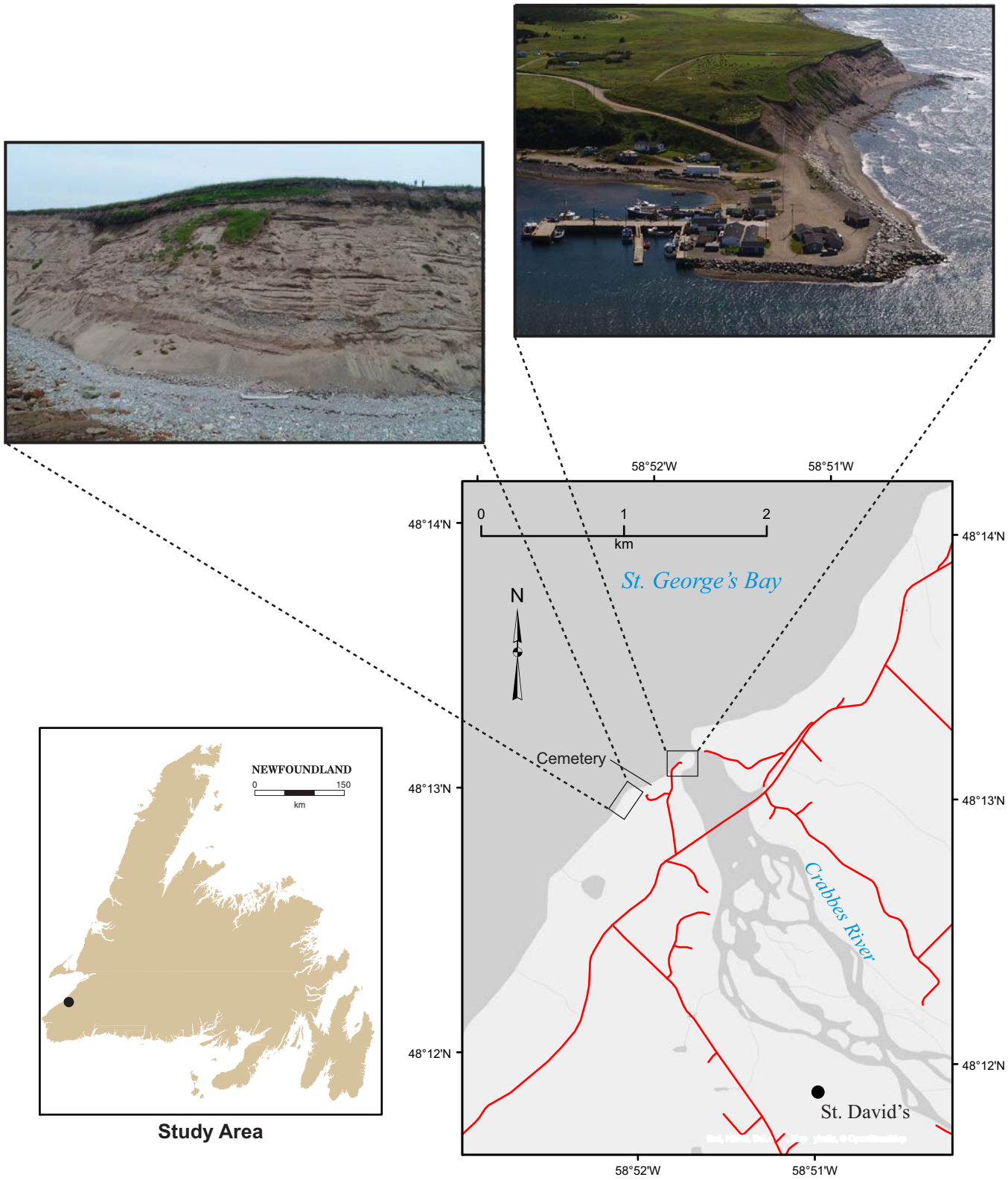

Figure 1. *Map of the St. David's area. The two photographs show the test areas: an eroding unconsolidated coastal cliff, and a low-lying beach and wharf area. The black dot shows the location of the study area.*

Plate 4. *The UAV Quadcopter Inspire 2 operator is holding the remote controller used to operate the UAV.*

mal wind speed (below 25 km/h), and an hour after sunrise and one hour before sunset, to ensure sufficient sunlight.

Prior to each flight, ground-control points (GCPs), readily discernible in the images, were placed on flat ground (Plate 5). A Leica GS09 RTK system with sub-centimetre accuracy, operating in survey mode, was used to obtain the exact location of the centre points of the targets.

Photogrammetry Methods

The UAV data were processed using Agisoft Photoscan™ Professional Version 1.3.4, which implements the Structure from Motion (SfM) photogrammetric technique.

Plate 5. *The Ground Control Points (GCPs) are of 30 by 30 cm black and white targets mounted on plywood. The operator is surveying the centre point of the GCP with the roving receiver of the RTK system.*

- First, images were aligned by scanning the images to detect points visible in more than one photograph (Plate 6A).

- Second, the location of the GCPs, as surveyed by the RTK, was imported into Photoscan and the location of the GCPs on photographs manually identified. The GCPs have two purposes: either as control points, or as

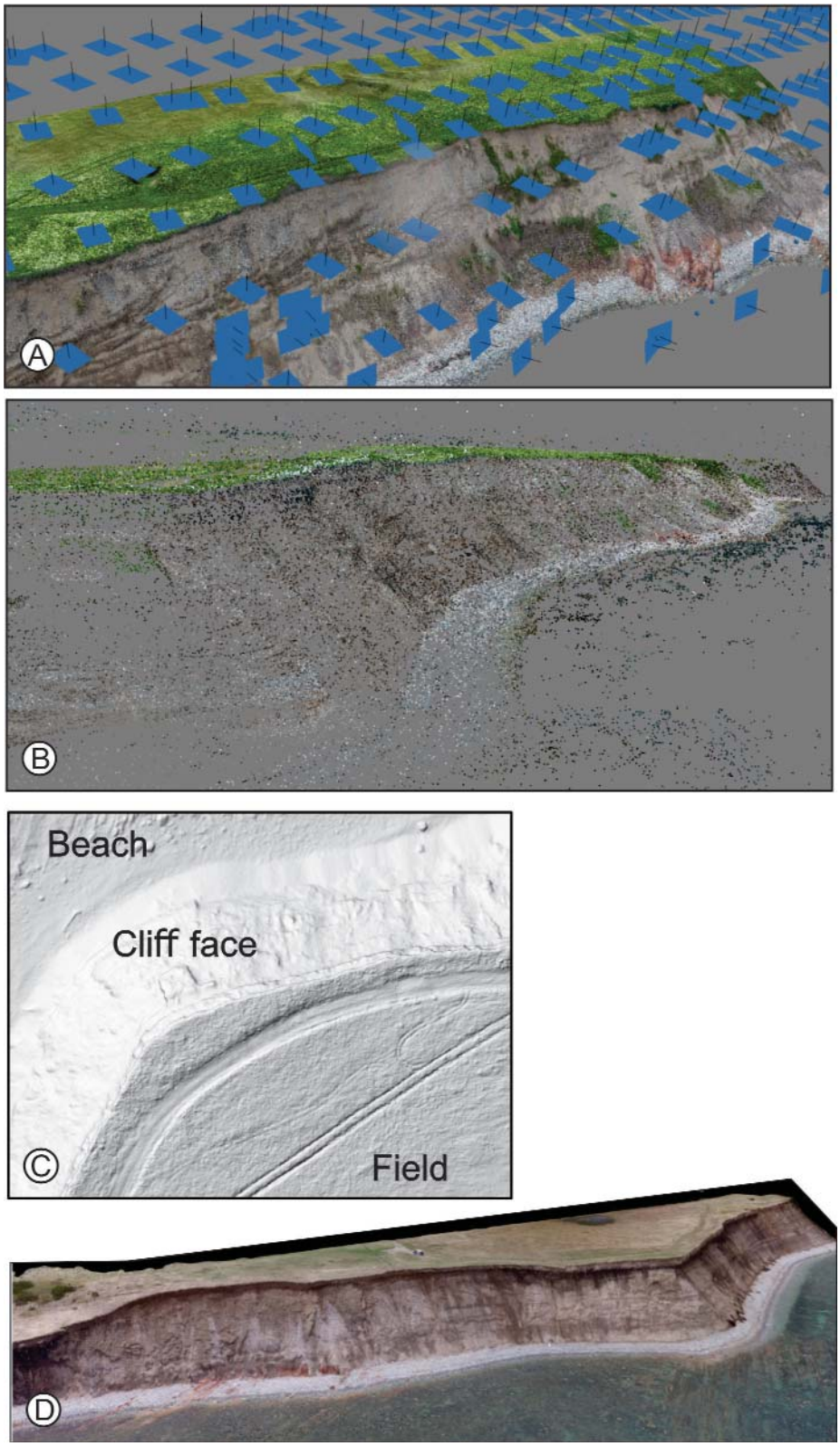

Plate 6. *A) Partial view of the textured 3-D surface of the coastal cliff. The blue rectangles show the positions of the photographs captured by the UAV in 2017, and the black lines the directions in which they were taken; B) Oblique view of the point cloud of the coastal cliff; C) Straight-down and close-up view of a greyscale representation of the DSM, with the sun's relative position taken into account for shading; D) A 3-D model of the cliff created from the 2016 UAV data.*

check points. Control points were used during data processing to remove non-linear distortions, and to adjust and georeference the model of the study area, created from the images into a real-world coordinate system. Check points were used to independently assess the accuracy of the model after data processing. As only a small number of GCPs were laid out during data collection in 2016, they were all used as control points. In 2017, 21 GCPs were laid out during data collection, and four trials were run, each one with different combinations of control and check points (Table 2).

Table 2. Numbers of GCPs used as control points and check points for the four trials of the 2017 UAV data

Trial #	# of check points	# of control points
1	21	0
2	15	6
3	10	11
4	4	17

- Third, a dense-point cloud, which is a set of data points in space defined by X, Y, and Z coordinates, and represents the external surface of the study area (Plate 6B); and a mesh, which consists of the vertices, edges and faces of the landscape, were created.

- Fourth, a Digital Surface Model (DSM), defined as a representation of the elevation of the Earth's surface including vegetation and infrastructure, was generated (Plate 6C).

- Fifth, an orthophotomosaic was generated by correcting the individual images for relief distortions and then projecting them onto a planimetric surface; a 3-D model was then created (Plate 6D). Projected data are expressed in the North American Datum 83 system.

The ground resolution (*i.e.*, the number of pixels per unit length) was superior in the 2017 flight data, compared with 2016; the improvement is explained by the lower flying altitude, and the model of UAV used (Table 1). Lower flying altitude results in increased ground detail being captured in the photographs, and the focal length of the camera on the DJI Inspire 2 is greater than that of the DJI Inspire 1, resulting in higher spatial resolution.

DSM Accuracy Analyses

To assess the accuracy of the model and to examine the influence of control points in data processing and select an optimal number thereof, four trials were run on the 2017 data, using differing combinations of control and check points (Table 2). The error in the X (easting), Y (northing) and Z (elevation) positions, and the Root-Mean-Square Error (RMSE) of the individual check points, as measured in the field by the RTK, compared to the data from the model, were determined (Table 3, Figure 2). The RMSE in the X, Y, and Z positions, and the total RMSE for all the check points used in each trial was also calculated (Table 4). The RMSE is defined as a resolution of the deviation, between the positions of the points measured by the RTK and the data from the model (Kršák *et al.*, 2016); the lower the RMSE value,

Table 3. Accuracy of the independent check points #2, 8, 11, and 21 for the four trials, run using the 2017 UAV data. The error, measured in cm, in the X, Y, Z positions, and the RMSE for each individual point are presented

Trial 1

	Error (cm)			
GCP #	X	Y	Z	RMSE
2	-166.519	3.574	108.498	198.779
8	-221.755	125.563	-39.7754	257.937
11	-185.524	15.6929	78.117	201.910
21	-134.662	-141.734	253.222	319.912

Trial 2

	Error (cm)			
GCP #	X	Y	Z	RMSE
2	-0.129	-0.425	3.287	3.317
8	-3.334	-5.38	-0.053	6.329
11	-2.43	-13.115	-0.576	13.351
21	0.16	-4.082	-1.323	4.294

Trial 3

	Error (cm)			
GCP #	X	Y	Z	RMSE
2	-1.033	0.446	2.746	2.968
8	-1.955	-6.721	-0.958	7.064
11	-5.439	-9.91	1.206	11.368
21	-1.269	-5.018	-2.686	5.832

Trial 4

	Error (cm)			
GCP #	X	Y	Z	RMSE
2	-0.019	2.653	1.181	2.904
8	-2.147	-6.763	0.085	7.097
11	-5.431	-6.287	-0.913	8.358
21	-1.803	-3.723	-1.21	4.31

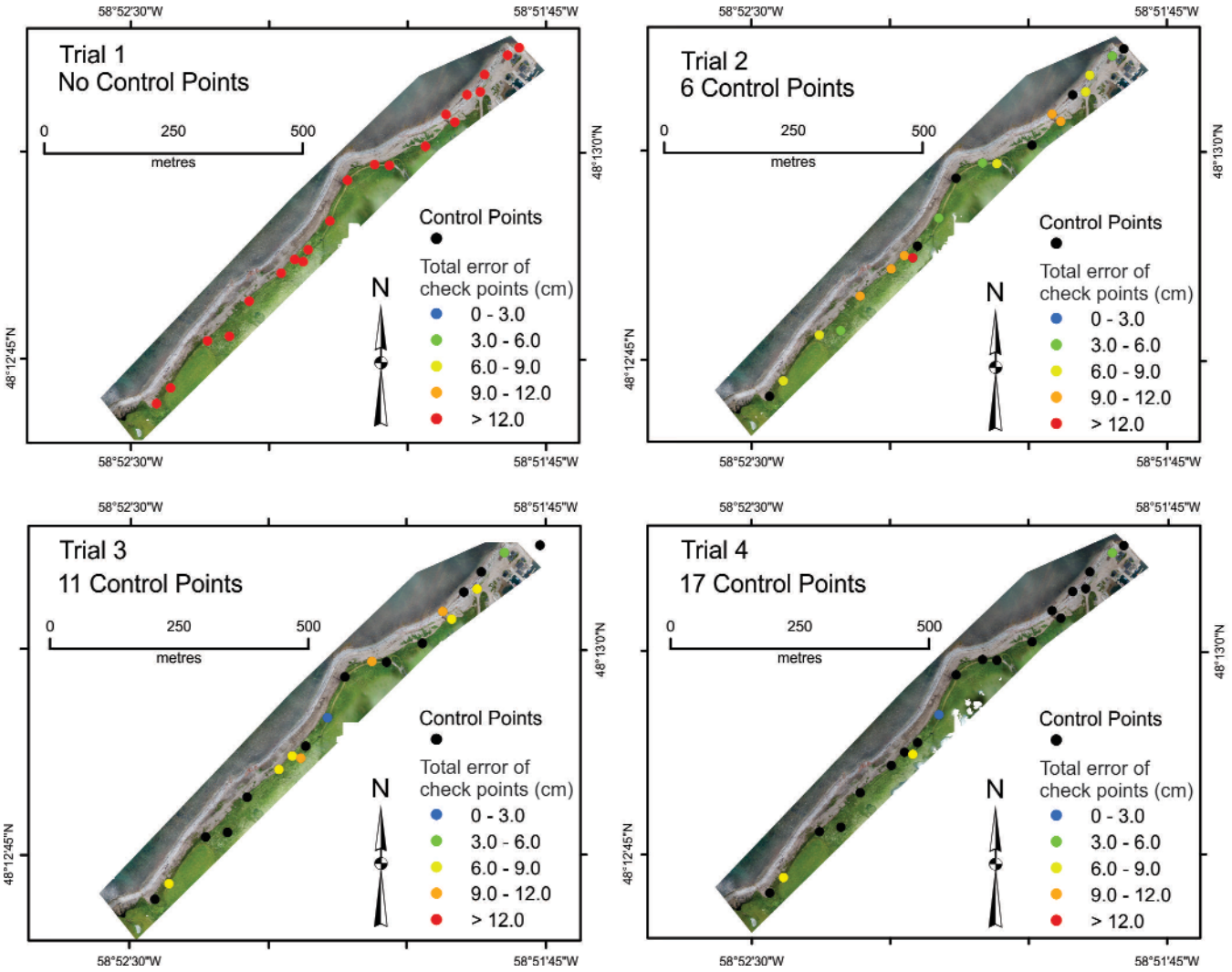

Figure 2. *Check point and control point locations for the four trials run using the 2017 data. Black dots represent the control points, and the total RMSE (in cm) of the check points is represented by circle colour.*

the more accurate the model is. The RMSE is calculated by the following formula (Agisoft, 2017):

$$RMSE = \sqrt{[(\sum_{i=1}^{i=n} x^2)/n]}$$

where x is the estimated error and n is the number of check points.

Surface Change

To study how the surface morphology has changed over time, two analyses were conducted. First, the rate of clifftop coastal erosion between 2013 and 2017 was calculated (Thieler *et al.*, 2009) as follows:

Table 4. Accuracy of all the control points used in each for the four trials, run using the 2017 UAV data. Error values are the RMSE, measured in cm, calculated for the X, Y, Z positions, and total RMSE for all of the control points processed; N is the number of control points used in the trial

	RMSE (cm)				
Trial #	X	Y	Z	Total	N
1	171.17	88.645	156.445	248.258	21
2	4.997	7.117	1.491	8.823	15
3	4.439	6.5956	1.618	8.113	10
4	3.056	5.152	0.962	6.067	4

1) The position of the clifftop in 2017 was digitized, based on the orthophoto and the DSM of the 2017 UAV data as processed in Trial 4. A model of the clifftop position was created from point data collected by the RTK in 2013. Trial 4 was chosen as the RMSE was lower compared to Trials 1-3 (*see* Results section below).

2) A baseline was created landward of the two clifftop positions.

3) The transect spacing was set to 1 m.

4) Shore-normal transects spaced at 1 m intervals were cast, extending from the baseline through the 2017 and 2013 clifftops.

5) Rates of shoreline change were determined based on points of intersection between the transects and the two clifftop positions and the End Point Rate (EPR) calculated; this is defined as the distance of total shoreline movement, divided by the time interval between the 2013 and 2017 measurement.

6) End point rates of erosion, as a function of distance along the clifftop, were overlain on the orthophoto (Figure 3).

Second, to quantify the changes in the cliff face, the DSM from 2017 was subtracted from that of 2016. These are shown in Figure 4, in which elevation changes are represented by a colour-coded scale indicating amount of change. In assigning colours, data were sorted into classes, each representing an interval of 20 cm; this classification size is greater than the estimated error in UAV data accuracy and ground resolution, and is an optimal size for displaying data trends for this study.

Modelling Flood-risk Mapping

Areas at risk of flooding due to potential sea-level rise to the year 2099 (Batterson and Liverman, 2010) were mapped by identifying all cells equal to or less than 1 m in height above high tide, which is measured at 1.6 m for the St. David's area (Fisheries and Oceans Canada, 2018). The 2017 DSM generated in Trial 4 was used; this trial was chosen as it has the lowest RMSE values, as described below. Areas at risk due to storm surges, in addition to sea-level rise, were mapped by identifying all cells between 1.01 and 3 m above high tide.

RESULTS

DSM ANALYSES

An assessment of the accuracy of the four DSMs created from the 2017 data is shown in Figure 2, and Tables 3 and 4. Ground Control Points # 2 and 11 had the lowest positional error in Trial 4, in which 17 control points were used in data processing. In Trial 2, in which 6 control points were

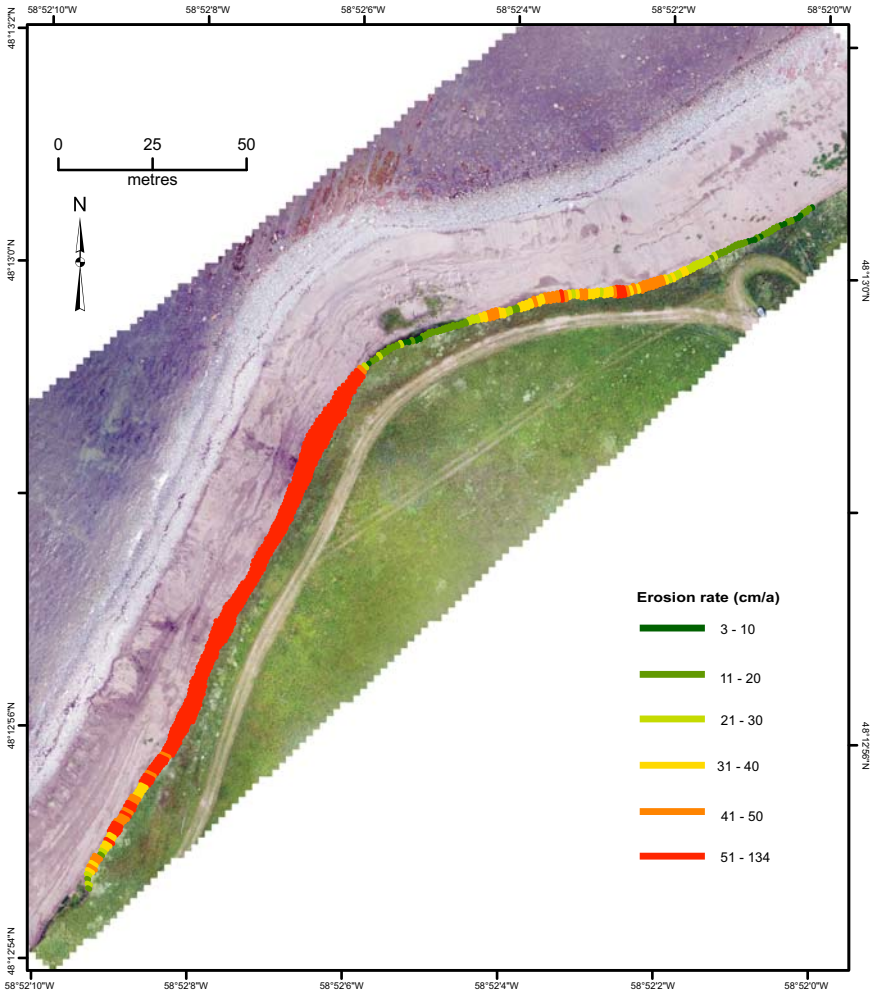

Figure 3. *Average annual rate of erosion from 2013 to 2017 along the coastline at St. David's. Colour and bar length represent the variation in erosion. The length of the bars represents the total amount (measured in cm) of clifftop erosion for the period of analysis; the greater the bar length, the greater the amount of coastal erosion.*

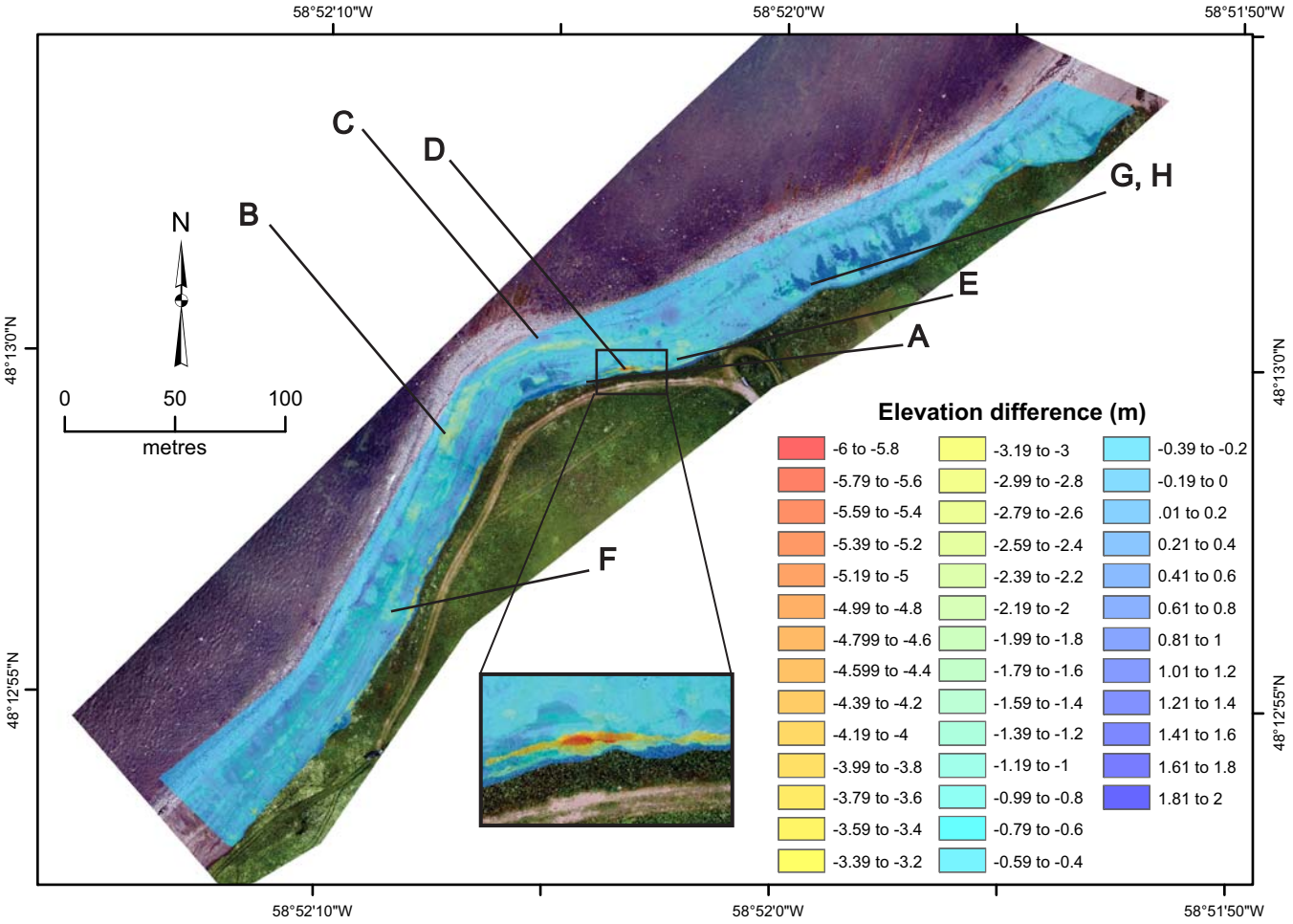

Figure 4. *Orthophoto showing elevation difference between the 2016 and 2017 UAV flights. Elevation changes are represented by a colour-coded scale showing amount of change; positive values denote elevation gain, and negative values denote elevation loss. Dark blue indicates areas of elevation gain, light blue indicates minimal change, and red indicates significant elevation loss and is enlarged to show detail. Letters refer to photos in Plate 7.*

used, GCP # 8 and 21 had marginally superior accuracies (less than a centimetre and less than a millimetre, respectively) compared to Trial 4 (Table 3). The model derived in Trial 4 is the most accurate as it has the lowest RMSE calculated for all the check points; total RMSE for all the check points was 6.07 cm (Table 4). Trials 2 and 3 had RSME's of 8.82 and 8.11 cm, respectively, whereas Trial 1 had a RMSE of 248.26 cm.

SURFACE CHANGE

Clifftop Erosion

Figure 3 shows the average rate of clifftop erosion between 2013 and 2017, measured in cm/a. The clifftop has eroded at an average rate of 52 cm/a; ranging between 3 and 134 cm/a. Erosion has been accelerated southeast of the point; here, the average rate of erosion has been 72 cm/a compared to 26 cm/a at the clifftop northwest of the point.

DSM Variance

The difference in DSMs from 2017 and 2016 indicates that overall, the cliff face has lost volume, which is consistent with field observations of erosion and changes in the position of the clifftop (Figure 4). By comparing the DSMs with field observations and images captured by the UAV, processes leading to erosion are identified (Plate 7). Elevation loss was accelerated along the clifftop in the central and southern part of the cliff, where the cliff is undercut (Plate 7A). Wind is causing erosion; the undercutting likely occurs due to wind tunnelling just below the overhang, removing the sand. If this process continues, the overhang will collapse. Waves removed sediment during high-water

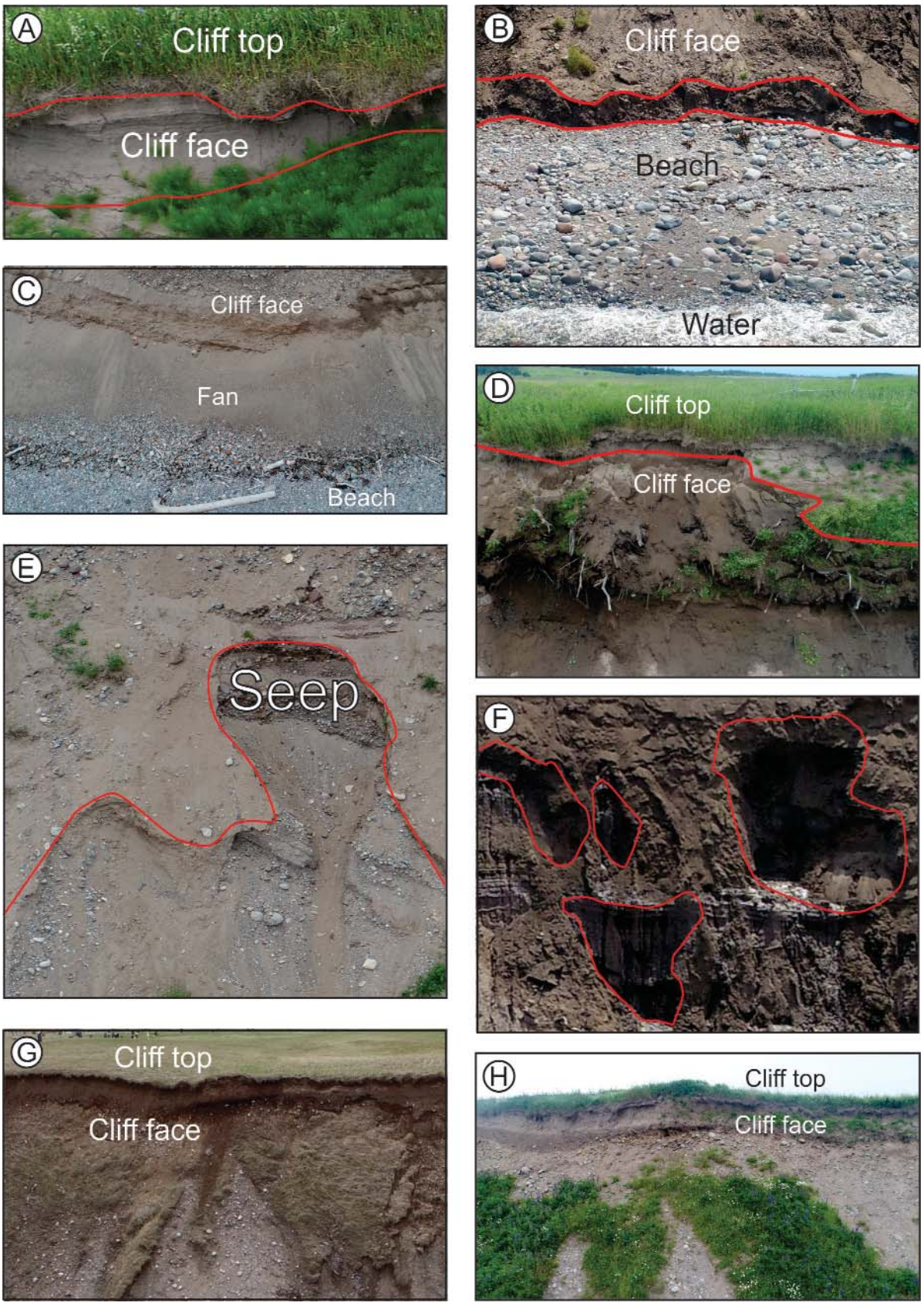

Plate 7. *Caption on page 27.*

along the cliff base southwest of the point (Plate 7B), but along the rest of the cliff base, colluvial material is present, indicating waves have not moved this material since its deposition, but have deposited driftwood. Both of these observations suggest that waves are not contributing significantly to erosion (Plate 7C). There has been accelerated erosion in the sand-rich pockets of the cliff face, compared to the gravel and clay-dominated layers, suggesting that surface water is flowing over the cliff face and removing the fine-grained material (Plate 7D). Groundwater has been exiting the cliff face above the clay-dominated layers, resulting in gulling (Plate 7E) and forming pipe-like erosion (Plate 7F). Areas of material increase are directly below gullies created by groundwater; sediment is being moved from where the water is exiting the cliff face, and deposited on the slope below. The presence of numerous seeps, gullies, rills and piping indicate groundwater flow is causing a significant quantity of erosion. There is an increase in the height of the vegetation during the 2017 survey, compared with 2016, in small vegetated pockets on the cliff face, and landward of the top of the cliff (Plate 7G, H).

DSM Flooding

The flood-risk map for St. David's shows areas at risk of flooding due to potential sea-level rise (by the end of this century) and are shown in areas coded yellow; they comprise portions of the lagoon side of the wharf area, and the base of the cliff (Figure 5). During a storm, surge waves could reach the base of the cliff, breach the boulder barrier and inundate the wharf area; these areas are coded red. Areas coded in blue are the present high-tide level.

DISCUSSION

The study shows that accurate (6.07 cm) and high-resolution models can be created from overlapping UAV images, which are processed using SfM and areas at risk to flooding

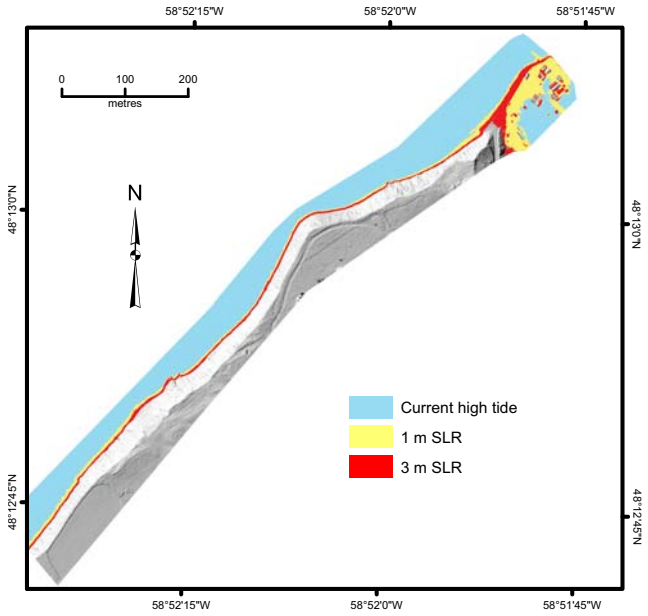

Figure 5. *Flood-risk map created from 2017 DSM data. Areas at risk of inundation due to sea-level rise are indicated in yellow, and areas at risk of inundation due to sea-level rise and storm surge in red. Areas at or below current high-tide level are indicated in blue.*

delineated. By conducting repeated UAV surveys of the same area, any changes in the morphology of the environment can be quantified.

The accuracy of the model is increased through the use of GCPs surveyed using an RTK system. One set of GCPs is incorporated during data processing as control points, whereas the other set is used as check points to independently estimate the error of the model. The number of control points influences the quality of the model reconstruction. When six or more control points were used, the RMSE measured from the check points was substantially lower

Plate 7 (page 26). *An examination of the images captured by the UAV and field-based observations led to the indication of factors resulting in elevation change, and are described in Plate 7A–H. Image location is identified by the corresponding letter on the orthophoto, and all images were captured at a 90° angle relative to the cliff. A) Image of the top of the cliff. Wind has removed sand from the top of the cliff face, creating a tunnel-like feature (outlined in red); B) Image of the base of the cliff, beach and water. Waves have removed sediment from the base of the cliff, as evident from the notch outlined in red; C) Image of the base of the cliff and beach. With the exception of the coastline southwest of the point (Plate 7B), there was no evidence of wave-based erosion; unconsolidated sediments eroded from the cliff have formed a fan, and waves have deposited driftwood along the base of the cliff; D) Image of the top of the cliff. The passage of surface water over the face of the slope has dislodged sand down the slope toward the base of the cliff (outlined in red); E) Image of a central area of the cliff face. When groundwater penetrates down to a dense clay layer, the downward movement is stopped, and water flows along the barrier to the cliff face, creating a seep. The water flowing from the seeps has removed sediment, resulting in the formation of gullies and rills (outlined in red); F) Image of the central area of the cliff face. Groundwater flowing from seeps has also created piping on the cliff face (outlined in red); G) Image of the central area of the cliff face, taken in 2016; H) Same portion of the cliff face as in G), photographed in 2017. The vegetation was higher in 2017 than in 2016, contributing to an increase in the apparent surveyed elevation of the cliff.*

than when no control points were used. Increasing the number of control points above six results in only a marginal decrease in the error. These findings are supported by other studies (Tonkin and Midgley, 2016, suggest a minimum of four control points; the Photoscan manual (Agisoft, 2017) recommends at least ten; and, Warrick *et al.* (2017) recommend six for the highest-quality results).

Tonkin and Midgley (2016) recommend an even distribution of control points over the study area, and Harwin and Lucieer (2012) argue for additional points in areas of high relief. However, the role of control-point distribution could not be assessed in the current study as the terrain limited the placement of GCPs, which must be placed on level surfaces. The steepest parts of the cliff were inaccessible, and boulders and cobbles on the beach, and tall, dense grass on the field landward of the cliff, prevented their placement. This may be an ongoing problem; however, it would be partly mitigated by surveying in the spring when vegetation growth is limited, allowing GCPs being placed in more of these areas.

James and Robson (2012) suggest a theoretical accuracy of 4 cm for a flight of 40 m above ground level. The values obtained in this study are higher (an overall accuracy of 6.07 cm, *see* Table 4), although similar to other studies; Lucieer *et al.* (2014) obtained total RMSE of 7.4 cm in the horizontal and 6.2 cm in the vertical, and Pineux *et al.* (2017) obtained accuracy values of 10–13 cm. Unlike studies by Lucieer *et al.* (2014), this study comprises oblique and straight-down photographs, and had a lower flight elevation than that employed by Pineux *et al.* (2017), which accounts for this study's superior data accuracy. The uneven distribution of GCPs could be the reason for the inferior accuracy of this study compared to the theoretical value suggested by James and Robson (2012).

The difference in the DSMs, and analyses of clifftop-erosion rates, indicate that most of the cliff face and overhead has been eroding and experiencing a loss of material; this is consistent with field observations. Comparison of the orthophotographs with the DSM variance indicates that a relationship can be established between the sediment type, wind, groundwater, and surface water, revealing that they are the main processes leading to erosion. Wave erosion has been limited to the coastline southwest of the point. Unfortunately, the DSM variance analysis suffers from a limitation, in that its measurements also incorporate seasonal elevation gains due to change in vegetation; whereas application of the same process using Digital Terrain Models (DTMs), for which Lidar imagery is necessary, involves the recording of differences in the surface of the unvegetated earth. However, the cost of Lidar puts it beyond this program.

Estimation of the accuracy of the proposed flood-risk areas' extent is beyond the scope of this study. St. David's has no published flood-risk maps, and no sources of oral or written flood history have been found; therefore, areas proposed in this study to be susceptible to flooding could not be compared with other models or past events. It is acknowledged that this study's method does not take into account sediment texture, slope or surface permeability in the flood-risk assessment; incorporation of these factors would improve the estimation of flood potential.

CONCLUSIONS

High-resolution photographs have been collected by repeated flights of a UAV over a beach, wharf and unconsolidated cliff at St. David's, western Newfoundland. Using Structure from Motion technique, overlapping oblique and vertical photos were processed to create point clouds, Digital Surface Models (DSM), 3-D models and orthophotos. Flying at an altitude of 40 m resulted in a ground resolution of 1.4 cm, and a Root Mean Square Error of 6.07 cm. Changes were quantified by comparing DSMs taken in different years, and by comparing the DSMs to existing topographic data collected with a Real Time Kinematics system. Between 2013 and 2017, the average rate of clifftop erosion has been 52 cm/a, and the cliff face has experienced erosion. The main coastal processes causing erosion have been identified as groundwater, surface water and wind. The high quality of the DSM allows for flood-risk mapping, due to sea-level rise and storm surges, in areas that previously lacked data of sufficient resolution to conduct such analyses. This shows that products created from UAV data are sufficiently robust to monitor coastal erosion and terrain stability, and to delineate areas of potential flooding.

ACKNOWLEDGMENTS

Gerry Hickey provided reliable logistical support. Steve Amor, Heather Campbell and Sarah Hashmi provided helpful reviews of earlier versions of the manuscript. The guidance, ideas and support provided by Martin Batterson and Larry Nolan are appreciated.

REFERENCES

Agisoft

2017: Agisoft Photoscan User Manual. Professional Edition, Version 1.3 Agisoft LLC, 111 pages.

Ajayi, O., Salubi, A.S., Angbas, A.F. and Odigure, M.G.

2017: Generation of accurate digital elevation models from UAV acquired low percentage overlapping images. International Journal of Remote Sensing, Volume 38, pages 3113-3134.

Batterson, M. and Liverman, D.
2010: Past and future sea-level change in Newfoundland and Labrador: Guidelines for policy and planning. *In* Current Research. Government of Newfoundland and Labrador, Department of Natural Resources, Geological Survey, Report 10-1, pages 129-141.

Batterson, M., Liverman, D. and Taylor, D.
1995: The assessment of geological hazards and disasters in Newfoundland. *In* Current Research. Government of Newfoundland and Labrador, Department of Natural Resources, Geological Survey, Report 95-1, pages 55-75.

2006: Geological disasters in Newfoundland and Labrador. Government of Newfoundland and Labrador, Department of Natural Resources, Geological Survey, Open File NFLD/2929, 94 pages.

Dail, H.J., Merrifield, M.A. and Bevis, M.
2000: Steep beach morphology changes due to energetic wave forcing. Marine Geology, Volume 162, pages 443-458.

Finnis, J.
2013: Projected impacts of climate change for the Province of Newfoundland and Labrador. Report submitted to the Office of Climate Change, Energy Efficiency and Emissions Trading, Government of Newfoundland and Labrador, 134 pages.

Fiorucci F., Cardinali, M., Carlà, R., Rossi, M., Mondinia, A.C., Santurri, L., Ardizzone, F. and Guzzetti, F.
2011: Seasonal landslide mapping and estimation of landslide mobilization rates using aerial and satellite images. Geomorphology, Volume 129, pages 59-70.

Fisheries and Oceans Canada
2018: Tides, currents and water levels. Online document, www.tides.gc.ca/eng

Forbes, D., Covill, R.A., Feindel, R.D. and Batterson, M.J.
1995: Preliminary assessment of coastal erosion between Port au Port and Stephenville, St. George's Bay, west Newfoundland. Geological Survey of Canada, Open File 3082, 49 pages.

Harwin, S. and Lucieer, A.
2012: Assessing the accuracy of georeferenced point clouds produced via multi-view stereopsis from unmanned aerial vehicle (UAV) imagery. Remote Sensing, Volume 4, pages 1573-1599.

Irvine, M.L.
2015: Monitoring coastal change in Newfoundland and Labrador: 2014 update. *In* Current Research. Government of Newfoundland and Labrador, Department of Natural Resources, Geological Survey, Report 15-1, pages 263-276.

James, M.R. and Robson, S.
2012: Straightforward reconstruction of 3D surfaces and topography with a camera: accuracy and geoscience application. Journal of Geophysical Research, Volume 117, F03017.

Kršák, B., Blištan, P., Pauliková, A., Puškárová, P, Kovanič, L., Palková J, and Zelizňaková, V.
2016: Use of low-cost UAV photogrammetry to analyze the accuracy of a digital elevation model in a case study. Measurement, Volume 91, pages 276-287.

Lucieer, A., de Jong, S.M. and Turner, D.
2014: Mapping landslide displacements using Structure from Motion (SfM) and image correlation of multi-temporal UAV photography. Progress in Physical Geography, Volume 38, pages 97-116.

Mancini, F., Dubbini, M., Gattelli, M., Stecchi, F., Fabbri, S. and Gabbianelli, G.
2013: Using unmanned aerial vehicles (UAVs) for high-resolution reconstruction of topography: the structure of motion approach on coastal environments. Remote Sensing, Volume 5, pages 6880-6898.

Pineux, N., Lisein, J. Swerts, G., Bielders, C.L., Lejeune, P., Colinet, G. and Degré, A.
2017: Can DEM time series produced by UAV be used to quantify diffuse erosion in an agriculture watershed? Geomorphology, Volume 280, pages 122-136.

Sallenger, A.H., Krabill, J.R., Swift, R.N., Brock, J., List, J. Hansen, M., Holman, R.A., Manizade, S., Sontag, J., Meredith, A., Morgan, K., Yunkel, J.K., Frederick, E.B., and Stockdon, H.
2003: Evaluation of airborne topographic Lidar for quantifying beach changes. Journal of Coastal Research, Volume 19, pages 125-133.

Razak, K.A., Straatsma, M.W., van Westen, C.J., Malet, J.P. and de Jong, S.M.
2011: Airborne laser scanning of forested landslides characterization: Terrain model quality and visualization. Geomorphology, Volume 126, pages 186-200.

Thieler, E.R., Himmelstoss, E.A., Zichichi, J.L. and Ergul, A.
2009: Digital Shoreline Analysis System (DSAS) version 4.0 – An ArcGIS extension for calculating shoreline change. U.S. Geological Survey, Open-File Report 2008, pages 1-79.

Tonkin, T.N. and Midgley, N.G.
2016: Ground-control networks for image based surface reconstruction: an investigation of optimum survey designs using UAV derived imagery and structure-from-motion photogrammetry. Remote Sensing, Volume 8, Issue 9, 786: doi:10.339olrs8090786.

Warrick, J.A., Ritchie, A.C., Adelman, G., Adelman, K. and Limber, P.W.
2017: New techniques to measure cliff change from historic oblique aerial photographs and Structure-from-Motion photogrammetry. Journal of Coastal Research, Volume 33, pages 39-55.

Watton, E.C.
2016: Coastal geomorphology, processes and erosion at the tourist destination of Ferryland, Newfoundland and Labrador. Unpublished M.Sc. thesis, Memorial University of Newfoundland, St. John's, 213 pages.

Westoby, M.J., Brasington, J., Glasser, N.F., Hambrey, M.J. and Reynolds, J.M.
2012: 'Structure-from Motion' photogrammetry: a low-cost, effective tool for geoscience applications. Geomorphology, Volume 179, pages 300-314.